Chemical Engineering Journal xxx (xxxx) xxx

Contents lists available at ScienceDirect

Chemical Engineering Journal

journal homepage: www.elsevier.com/locate/cej

Toward high-performance and flexible all-solid-state micro-supercapacitors: MOF bulk *vs.* MOF nanosheets

Fangna Dai [a], Xiaokang Wang [a], Shuanghao Zheng [b,c], Jianpeng Sun [a], Zhaodi Huang [a], Ben Xu [a], Lili Fan [a], Rongming Wang [a], Daofeng Sun [a,*], Zhong-Shuai Wu [b,c,*]

[a] School of Materials Science and Engineering, College of Science, China University of Petroleum (East China), Qingdao, Shandong 266580, China
[b] State Key Laboratory of Catalysis, Dalian Institute of Chemical Physics, Chinese Academy of Sciences, 457 Zhongshan Road, Dalian 116023, China
[c] Dalian National Laboratory for Clean Energy, Chinese Academy of Sciences, 457 Zhongshan Road, Dalian 116023, China

ARTICLE INFO

Keywords:
Metal-organic frameworks
Porphyrin ligand
Ultrathin nanosheet
Micro-supercapacitors
Energy storage

ABSTRACT

Due to the advantages of ultrahigh power density, long lifespan and easy integration with wearable and microscale electronics, micro-supercapacitors (MSCs) have attracted great interest in recent years. However, new high-performance electrode materials for such micro-electrochemical energy storage devices require deep excavation. Herein, we precisely synthesized a new 3D bulk MOF and new 2D ultrathin MOF nanosheets with a thickness of less than 10 nm, and utilized them as high-capacitance microelectrode materials for sophisticated all-solid-state MSC devices respectively. Notably, the MSCs based on MOF nanosheets displayed a high areal capacitance of 28.3 mF·cm^{-2}, and a volumetric capacitance of 15.7 F·cm^{-3} at 0.2 mA·cm^{-2}. Especially, our MSCs exhibited remarkable energy density of 8.7 mWh·cm^{-3} at a power density of 110.3 mW·cm^{-3}, and excellent cycling lifespans with retention of 96.0% after 10,000 cycles, and all performances are better than the MSCs based on MOF bulks. This work provides a new way to further explore the inherent advantages of MOFs and stimulates the synthesis of advanced MOFs materials for application in microscale energy storage.

1. Introduction

Microscale electrochemical energy storage devices have attracted considerable attention due to the advantages of light weight, foldability, and facile manipulation [1–3]. Supercapacitors are promising energy storage devices owing to the high power density, long cycle stability, and moderate energy density [4–6]. In particular, micro-supercapacitors (MSCs) demonstrate great potential applications as wearable energy storage devices with their excellent mechanical strength and micro-miniaturization [7,8]. Although MSCs have been greatly improved in recent years, the insufficiency of electrode materials still hinders their practical application. For instance, the most commonly used carbon-based materials can barely satisfy the requirements for high energy density. Hence, it is vital to develop highly flexible and high-capacitance electrode materials to boost energy density [9,10].

Metal-organic frameworks (MOFs), constructed from organic ligands and metal ions, have showed significant advantages owing to their uniformly dispersed metal centers and adjustable functional groups [11,12]. Compared with conventional porous materials (such as carbon and zeolites), the high surface area and ordered porosity of three-dimensional (3D) and two-dimensional (2D) MOFs are conducive to ion transport [13,14]. With the concern of energy issues, more and more works began to focus on the application of MOF materials in the field of energy storage. For example, Bao *etc.* have constructed supercapacitors using redox-active conductive 2D MOFs as electrodes with aqueous electrolytes [15]. A conjugated copper(II) catecholate MOF were used in symmetric solid-state supercapacitors [16]. The most famous 2D conductive $Ni_3(HITP)_2$, $Cu_3(HITP)_2$ serials were also utilized in supercapacitors [17]. Recently, Feng and Kornyshev *et al.* performed constant-potential molecular dynamics simulations to analyze the electric double-layer structure and capacitive performance of 2D conductive MOF electrodes for supercapacitors [18]. It is predicted that 3D conductive MOF scaffolds are expected to have advantages over the dense stacks of 2D MOF sheets with quasi-1D pores. It is true that 3D scaffolds can provide a full range of ion transport paths to enhance the charging dynamics and energy and power density of traditional

* Corresponding authors at: School of Materials Science and Engineering, College of Science, China University of Petroleum (East China), Qingdao, Shandong 266580, China (D.F. Sun), State Key Laboratory of Catalysis, Dalian Institute of Chemical Physics, Chinese Academy of Sciences, 457 Zhongshan Road, Dalian 116023, China (Z.-S. Wu).
E-mail addresses: dfsun@upc.edu.cn (D. Sun), wuzs@dicp.ac.cn (Z.-S. Wu).

https://doi.org/10.1016/j.cej.2020.127520
Received 21 July 2020; Received in revised form 13 October 2020; Accepted 23 October 2020
Available online 12 November 2020

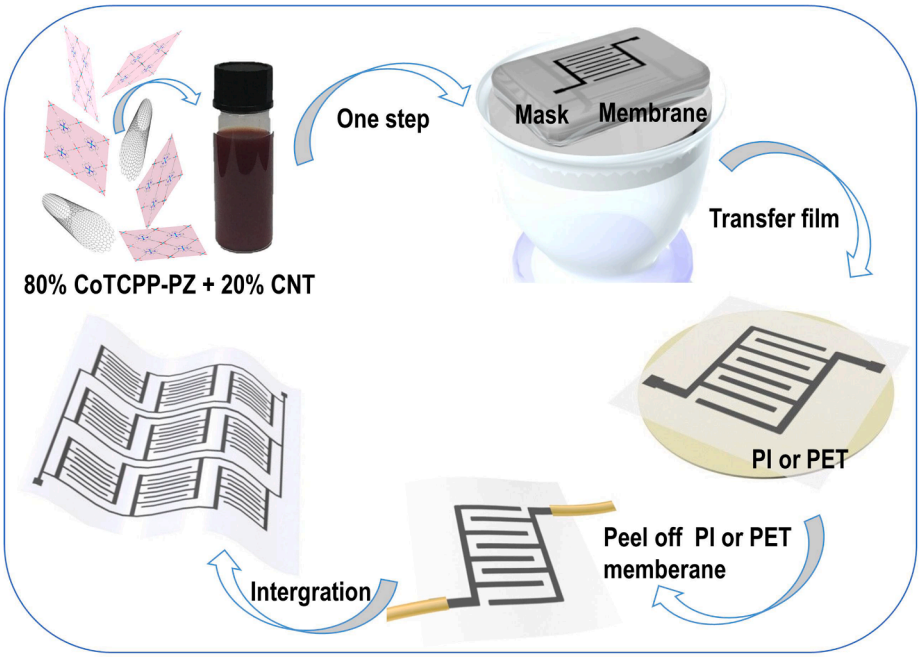

Fig. 1. Scheme of 2D MOF nanosheets for flexible MSCs *via* mask-assisted simplified fabrication.

supercapacitors. However, traditional sandwich-like supercapacitors with a stacked structure are difficult to fully maximize the rate performance of MOF materials. Also, whether it is either 2D MOF or 3D MOF mentioned above, they suffer from the poor adhesion, which would hinder their application in electrical devices [19].

It is meaningful to do a deep excavation for MOF materials from structure to morphology, especially from 3D MOF bulks (focus on structure) to 2D MOF nanosheets (focus on morphology) [20–24]. For example, flowerlike bimetallic MOF nanosheets grown on the electrospun nanofibers [25], and a layered Co-based metal-organosulfide coordination polymers nanosheet array supported on a nickel foam substrate were used in asymmetric supercapacitors [26]. It should be noted that all the works reported above were based on traditional stacked supercapacitors, rather than planar MSCs. If MOFs can take full advantage of the unique nature of functional motifs and achieve reasonable control at molecular level, their direct application in microdevices will open up a new avenue.

Ultrathin MOF nanosheets can achieve large exposed surface area, abundant accessible active sites, high surface-to-volume atom ratios, atomic or molecular thickness, and robust mechanical strength [27–29], which will be well-matched to the co-plane configuration of MSCs. Meantime, the electrolyte ions can be transferred along the parallel plane of 2D MOF nanosheets with smaller diffusion barriers, and the atomic thickness can be fully utilized to adequately improve the electrochemical performance, which is very suitable for MSCs. Based on the above expectations, we have designed two sophisticated all-solid-state MSC devices in this work. First, a new 3D bulk MOF [Co_2(CoTCPP)$(PZ)_2$] (named CoTCPP-PZ bulk, H_6TCPP = 5,10,15,20-tetra(carboxyphenyl) porphyrin, PZ = pyrazine) was constructed based on porphyrin and pyrazine ligands. Following a surfactant-assisted bottom-up synthetic method, the growth of MOF was restricted to a certain plane, and the 2D ultrathin CoTCPP-PZ nanosheets with a thickness of less than 10 nm were successfully isolated. Through a one-step mask-assisted, simplified fabrication strategy [30], the MOF nanosheets or MOF bulk are successfully employed as free-standing electrode materials, and the MN-MSCs (denoted for MOF-nanosheets-based MSCs) and MB-MSCs (denoted for MOF-bulk-based MSCs) with the interdigital electrode patterns are achieved (Fig. 1). When working in the ionic liquid electrolyte of $EMIMBF_4$ (1-ethyl-3-methylimidazolium tetrafluoroborate), MN-MSCs deliver a high areal capacitance of 28.3 mF·cm^{-2}, and volumetric capacitance of 15.7F·cm^{-3} at 0.2 mA·cm^{-2}. Furthermore, the fabricated devices exhibit a high energy density of 8.7 mWh·cm^{-3}, and have excellent cycling lifespan with retention of 96.0% after 10,000 charge/discharge cycles, all of which are better than MB-MSCs. In addition, MN-MSCs are highly flexible, permitting scalable production of parallel and serial interconnected modular power sources for designable integrated circuits with high output current and voltage.

2. Experimental

2.1. Materials

The H_6TCPP (5,10,15,20-tetra(carboxyphenyl) porphyrin) ligand, $CoCl_2{\cdot}6H_2O$, PZ (pyrazine), HCl, HNO_3, $HClO_4$, PVDF (vinylidene fluoride, Mw = 180,000), $EMIBF_4$ (1-ethyl-3-methylimidazolium tetrafluoroborate, ≥99.0% (HPLC)), 4-methyl-2-pentanone (MP, ≥99.5%, HPLC), and propylene carbonate (PC, ≥99.0%, GC) were purchased from Sigma-Aldrich. EtOH (ethanol, 99.9%) was purchased from Merck. Dimethylacetamide (DMA) was purchased from Fisher Scientific. CNT (~15 μm) was purchased from Chengdu Organic Chemicals Co. Ltd. All the chemicals were used as received without further purification.

2.2. Synthesis of CoTCPP-PZ bulk [Co_2(CoTCPP)$(PZ)_2$]·6DMA·2H_2O

$CoCl_2{\cdot}6H_2O$ (10.0 mg, 0.04 mmol), H_6TCPP (10.0 mg, 0.01 mmol), PZ (5.0 mg, 0.13 mmol), DMA (1.0 mL) and $HClO_4$ (50.0 μL) were heated to 120 ℃ for 24 h in a sealed tube. The red crystalline block formed on the walls of the glass tube was collected by filtration, washed with DMA and EtOH and dried in air (yield: 65%, based on cobalt). Elemental analysis Calcd for $Co_3C_{80}H_{110}N_{14}O_{23}$ (%): C, 53.02; H, 6.07; N, 10.82. Found: C, 53.61; H, 6.91; N, 10.07.

2.3. Synthesis of CoTCPP-PZ nanosheet [Co_2(CoTCPP)$(PZ)_2$]·3EtOH

$CoCl_2$ 6H_2O (5.0 mg, 0.02 mmol), H_6TCPP (2.5 mg, 0.006 mmol), PZ (2.5 mg, 0.03 mmol), DMA (10.0 mL), $HClO_4$ (25.0 μL) and PVP (10.0 mg, Mr = 40000) were heated to 120 ℃ for 3600 min in a sealed tube, followed by slow cooling to room temperature over 10 h. Yield: 2.0 mg

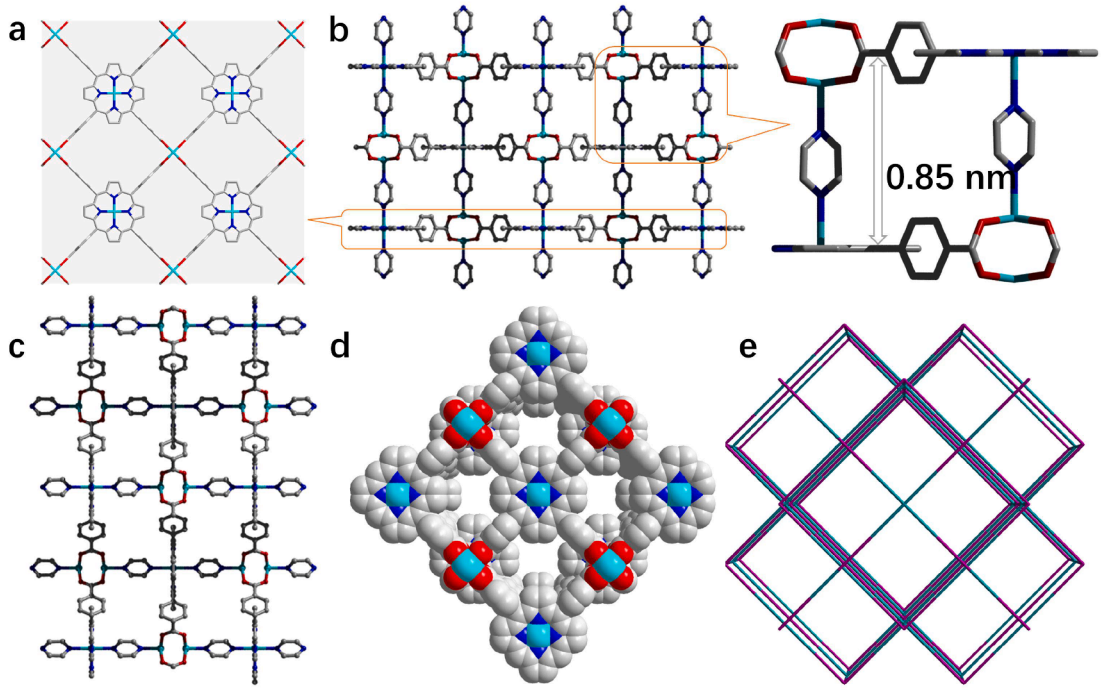

Fig. 2. a) The layer structure in CoTCPP-PZ. b) and c) The pillar-layered structure viewed along the *b* and *a* axes. d) and e) Pores and *pcu* topology viewed along the *c* axis.

(40% based on cobalt). Anal. Calcd for $Co_3C_{62}H_{56}N_8O_{11}$ (%): C, 58.83; H, 4.43; N, 8.86. Found: C, 58.0; H, 4.98; N, 9.01.

Thermogravimetric analysis (TGA) curves display approximately 37.1% weight loss in the temperature range from 40 °C to 375 °C (Fig. S1 in Supporting information), which is assigned to the release of guest water molecules and DMA molecules for CoTCPP-PZ bulk, as compared with 16.8% weight loss due to the release of three guest ethanol molecules for CoTCPP-PZ nanosheet. Above 375 °C, both frameworks start to decompose.

2.4. Preparation of ionic liquid gel electrolyte

The PVDF/$EMIBF_4$ gel electrolyte was chosen as the gel electrolyte for our solid-state supercapacitors. Typically, 1.0 g PVDF was mixed with 1.0 g $EMIBF_4$, with 10.0 mL MP and 2.5 g PC subsequently added into the ionic liquid solution. The mixture was reflux and stirred vigorously for complete solvation and homogeneous mixing at ~80 ℃ for 2 h.

2.5. Fabrication of MN-MSCs and MB-MSCs

To fabricate this interdigital film electrode, a customized interdigital mask with four fingers (length of 14.0 mm, finger width of 1.0 mm) on each side was manufactured to define the patterned geometry. Prior to electropolymerization, the CNT was treated with 1.0 mol·L^{-1} HNO_3 (aq) and then 1.0 mol·L^{-1} HCl (aq) for 12 h, followed by a thorough rinse with deionized water and dry at 50 ℃. The stable ink of 4.0 mL methanol dispersions of CoTCPP-PZ nanosheets (0.1 mg·mL^{-1}) and CNT with a mass ratio of 80:20 was filtered through a PTFE membrane (pore size 0.45 μm) by mask-assisted vacuum filtration, and then a thin layer of CNT film (about 2.0 μm) of the interdigital electrode was suction-filtered as a conductive substrate. After that, the resultant patterned hybrid film was directly dry transferred to a 12.5 μm-thick PI (Polyimide) or PET (Polyester) substrate with the assistance of 20.0 MPa pressure to obtain CoTCPP-PZ nanosheets interdigital electrodes. To completely remove the residual methanol, CoTCPP-PZ nanosheets electrodes were placed into a vacuum oven for 12 h at 60 °C and then transferred into an argon-filled glovebox (MBraun Labstar, with less than 0.5 ppm of oxygen and water). $EMIBF_4$ ionic liquid gel electrolyte was then slowly drop-casted onto the surface of interdigital electrodes. Finally, the device was covered by the other Kapton film and was sealed by AB glue. For comparison, we also fabricated the MB-MSCs by one-step filtration using CoTCPP-PZ bulks and CNT with the mass ratio of 80:20 as the electrodes.

2.6. Material characterization

Transmission electron microscopy (TEM) images, high-resolution TEM (HRTEM) image, dark-field scanning TEM-energy dispersive X-ray spectroscopy (DF-STEM-EDS) and elemental mappings were taken on a JEOL JEM2100F microscope, equipped with EDS. Selected area electron diffraction (SAED) patterns were recorded by JEOL JEM-2010UHR. X-ray diffraction (XRD) patterns were recorded with a Panalytical X-ray diffractometer, using Cu Kα radiation (λ = 1.5406 Å). The thickness of nanosheets was characterized by atomic force microscopy (AFM, Cypher, Asylum Research). Thermo-gravimetric analysis (TGA) experiments were performed on a Mettler Toledo instrument at a heating rate of 10 °C min^{-1} over the range of 40–800 °C under an N_2 atmosphere. FT-IR spectra were recorded in the range of 4000 cm^{-1} to 500 cm^{-1} by using a PerkinElmer Frontier FT-IR Spectrometer. Elemental analyses (C, H, and N) were carried out using a Perkin-Elmer 2400 CHN elemental analyzer.

2.7. Electrochemical characterization

Cyclic Voltammetry (CV) and Galvanostatic charging-discharging (GCD) were conducted using the CHI 660d potentiostat (Shanghai Chenhua) and Solartron (AMETEK. Inc.). Electrochemical performance of PI composite electrode was characterized in the ionic liquid of $EMIMBF_4$ using an electrochemical workstation in a three-electrode configuration, where Pt is a counter electrode, Ag/AgCl is reference electrode and the composite electrode is the working electrode. For the electrochemical characterization of flexible supercapacitors, the Solartron (AMETEK. Inc.) was used. Specific areal and volumetric capacitances were determined using the CV and CP curves. Specific volumetric

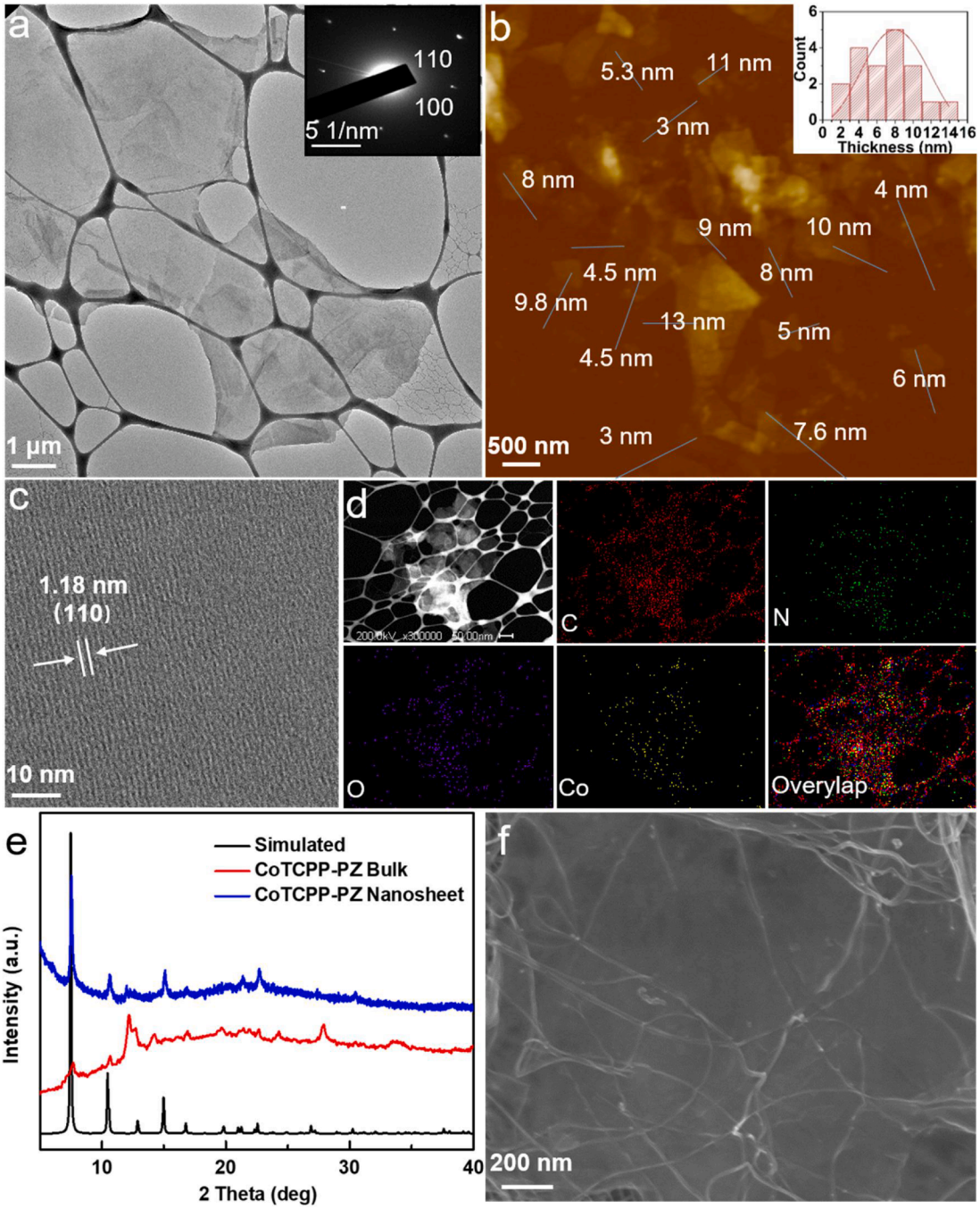

Fig. 3. Characterization of 2D ultrathin CoTCPP-PZ nanosheets. a) TEM image, SAED pattern (insert). b) AFM image. c) HRTEM image and d) DF-STEM-EDS elemental mapping. e) PXRD patterns. f) SEM image from the top surface of MN-MSCs.

capacitances (CV-GV, $mF{\cdot}cm^{-3}$) is based on the total volume of the supercapacitors. The impedance spectra were recorded in the frequency range from 10,000 to 0.01 Hz with a sinusoidal excitation signal of 10 mV at the open circuit potential.

3. Results and discussion

CoTCPP-PZ bulk crystallizes in a tetragonal *I4/mmm* space group and the asymmetric unit consists of two crystallographically unique Co(II) ions (Co1 and Co2), one-eighth of the deprotonated TCPP anions, and half of a PZ molecule (Table S1). Each Co1 ion is coordinated by four carboxylate oxygen atoms from four TCPP ligands, and one PZ molecule, forming a Co_2 paddlewheel SBU with an adjacent Co1 ion. Each TCPP is connected to four Co_2 paddlewheel nodes through carboxylate groups to produce a 2D layered structure (Fig. 2a). Each Co2 ion links to four nitrogen atoms from TCPP, forming a TCPP(Co) unit, with two PZ molecules to form a CoN_6 octahedron. Thus, the PZ ligands bridging Co1 and Co2 ions, further connect the 2D layers to form a pillar-layered 3D structure (Fig. 2b-2d, with a layer separation of 0.85 nm). A PLATON calculation reveals that the total solvent-accessible volume of CoTCPP-PZ is 2674.5 $Å^3$ per unit cell, and accounts for approximately 56.7% of the cell volume. Topologically, the Co_2 paddlewheel SBU and TCPP (Co) can both be regarded as 6-connected nodes, thus forming a 6-connected ***pcu*** alpha-Po primitive cubic net with the point symbol of $\{4^{12}.6^3\}$, as calculated by TOPOS (Fig. 2e) [31].

Dimensionally reducing 3D bulk MOFs into 2D nanosheets could be

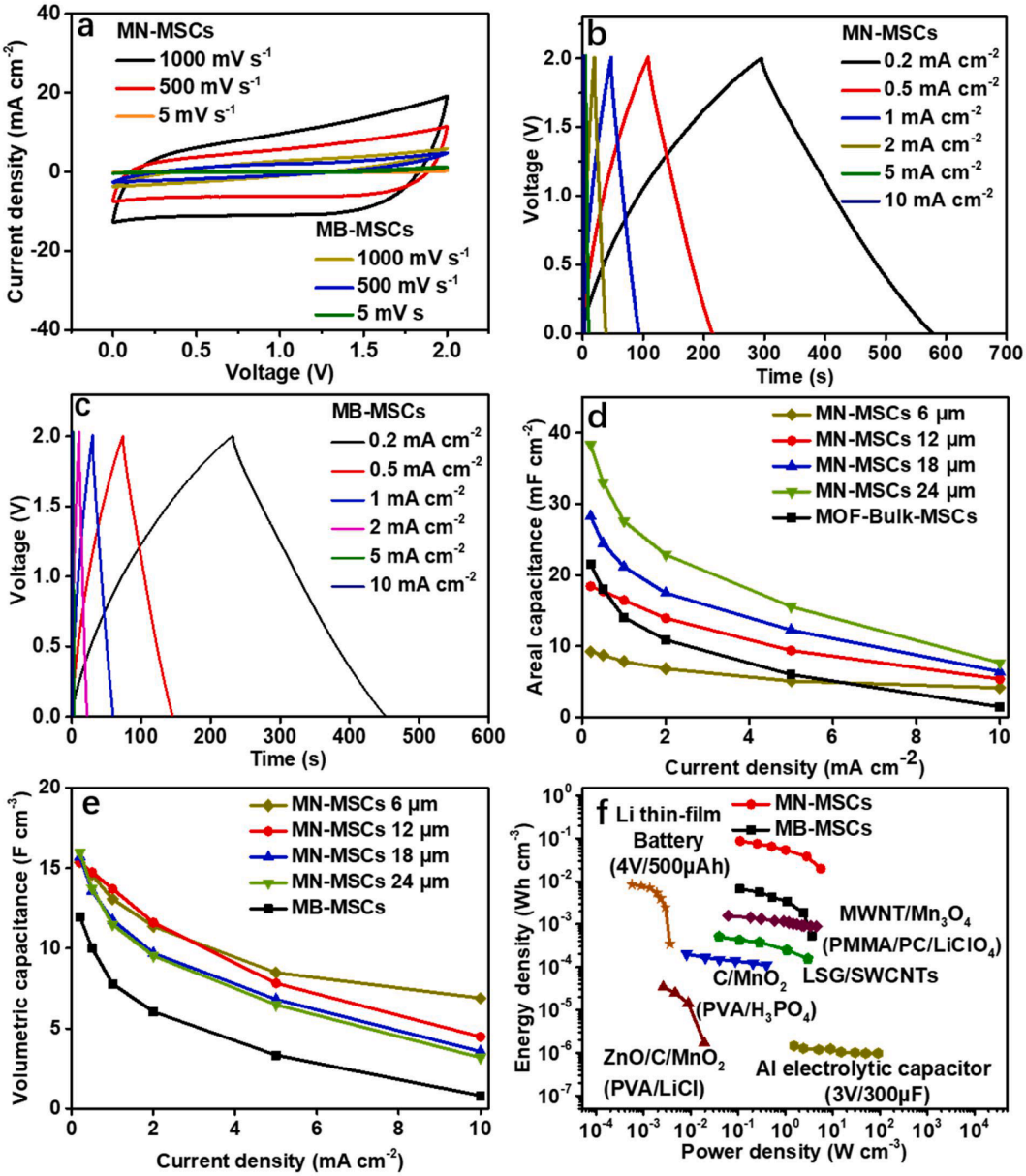

Fig. 4. Electrochemical performances of MN-MSCs and MB-MSCs. a) The CV curves and typical GCD profiles. b) MN-MSCs with a MOF nanosheets electrode thickness of 18 μm and c) MB-MSCs. d) The areal and e) volumetric capacitance with different thicknesses at different current densities. f) Ragone plot of MSCs compared with other microscale energy storage devices.

an effective strategy to reduce the ion penetration pathway and support applications in electronic devices. The surfactant-assisted bottom-up method has been successfully utilized to obtain ultrathin CoTCPP-PZ nanosheets. The bright-field TEM image clearly reveals that the lateral size of the CoTCPP-PZ nanosheets is 2.6 ± 0.6 μm (Fig. 3a). The diffraction spots observed in the selected-area electron diffraction (SAED) patterns collected along the [0 0 1] (Fig. 3a, inset) are attributed to the (1 1 0) and (1 0 0) planes of the nanosheets. The thickness of CoTCPP-PZ nanosheets (6.6 ± 2.0 nm) was measured by atomic force microscopy (AFM) (Fig. 3b). Based on the single crystal structure shown in Fig. 1b, the theoretical interlayer distance of CoTCPP-PZ is estimated to be 0.85 nm and the layer number of obtained CoTCPP-PZ nanosheets is approximately 7 ± 2. The lattice fringes of the CoTCPP-PZ nanosheets are characterized by high-resolution TEM (HRTEM), which indicates that its excellent stability and an interplanar distance of 1.18 nm (Fig. 3c) are ascribed to the (1 1 0) plane of CoTCPP-PZ. The compositions of the nanosheets are examined by dark-field scanning TEM-energy dispersive X-ray spectroscopy (DF-STEM-EDS), which demonstrates that C, N, O, and Co are uniformly distributed in the nanosheets (Fig. 3d). The PXRD pattern (Fig. 3e), Fourier transform infrared (FTIR) spectroscopy, and thermogravimetric analysis (TGA) curves were performed (Fig. S1-2), and proved the consistency of the CoTCPP-PZ bulk and the CoTCPP-PZ nanosheets.

The Brunauer–Emmett–Teller (BET) surface area of CoTCPP-PZ Bulk is 175 m^2/g, significantly lower than that of CoTCPP-PZ nanosheet for 431 m^2/g (Fig. S3). The pore size distribution indicates that both of nanosheets and bulks have the same micropores of 0.65 nm and mesopore pores with size range of 2.05 ~ 2.75 nm, which could be attributed to the slit-like pores formed by aggregation. 2D CoTCPP-PZ nanosheets with extended lateral dimensions, nanometer thickness, and electronic conductivity of 7.7×10^{-4} $S \cdot cm^{-1}$ (Fig. S4) possess numerous accessible active sites on their surfaces and are expected to exhibit excellent performance in MSCs. To demonstrate this, the stable ink of CoTCPP-PZ nanosheets and carbon nanotube (CNT) with a ratio of 80:20 was

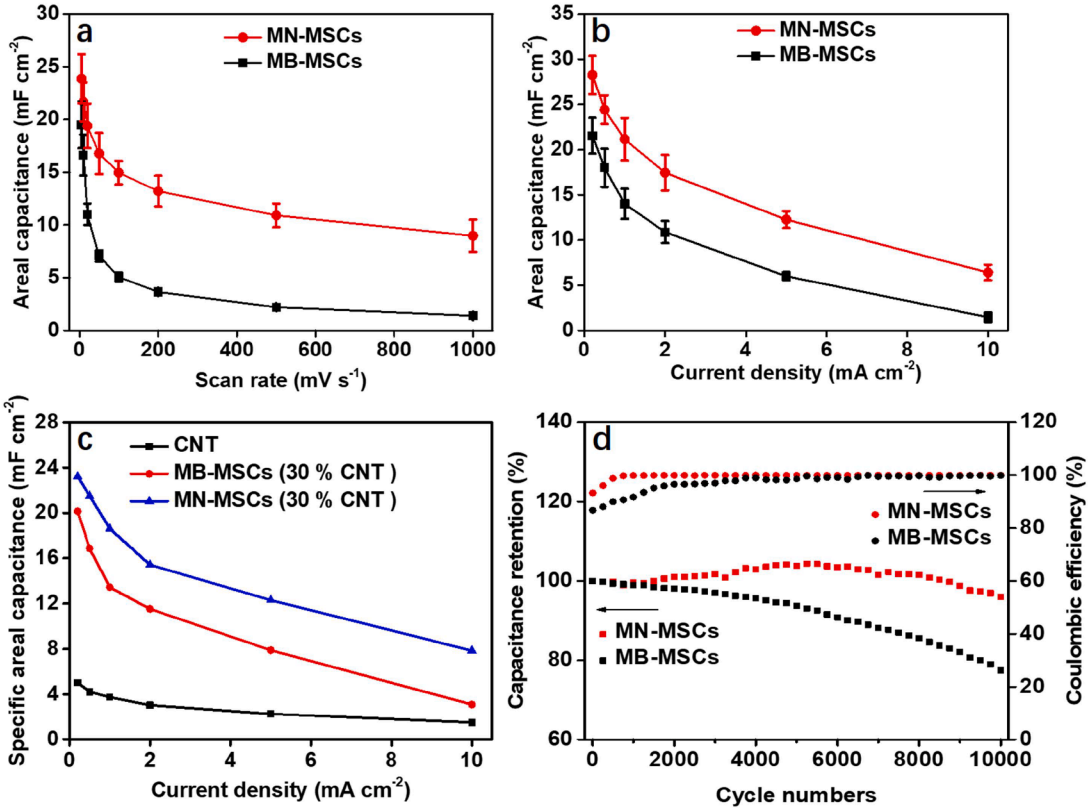

Fig. 5. Areal capacitances of the MSCs at different a) scan rates and b) current densities. c) Areal capacitances of CNT and MSCs with 30% CNT at different current densities. d) Cycling stability and coulombic efficiency of MSCs obtained at 5 mA·cm^{-2}.

filtered through a polytetrafluoroethylene (PTFE) membrane (pore size 0.45 μm) through a mask-assisted vacuum filtration to construct the interdigital microelectrodes of MN-MSCs. Afterwards, the fabricated patterned film was transferred onto a polyimide (PI) or polyester (PET) substrate (with a thickness of 6 ~ 24 μm) and integrated it into the interdigital pattern, as shown in Fig. 1. The ionic liquid of $EMIMBF_4$ was utilized as the electrolyte and casted on the planar patterned microelectrodes. The planar MN-MSCs were finally obtained after device packaging, and Fig. 3f showed the SEM image from the top surface of MN-MSCs. Compared with multiple-step lithographic processing, *e.g.*, O_2 plasma etching and photoresist, this method can efficiently avoid solvent contamination, and needn't separator or adhesives, that is critical for maximizing charge storage of the 2D nanosheets on the interdigital electrodes along the coplanar substrate, such a simplified manufacturing method is beneficial for highly flexible scalable device integration [30].

To further illustrate the advantages of lamellar nanosheets as the electrode material of MSCs (MN-MSCs), we also fabricated MSCs using the initial 3D bulk MOF (MB-MSCs). The electrochemical performances of MN-MSCs and MB-MSCs were measured and compared with a voltage of 2 V employing cyclic voltammetry (CV) measurements at different scan rates ranging from 5 to 1000 mV·s^{-1} (Fig. 4a). The CV patterns of MN-MSCs are rectangular, and the ion liquid as electrolyte is quite stable, preventing the redox reactions of Co^{2+}/Co^{3+} between electrodes and electrolyte. Therefore, the charge storage behavior of CoTCPP-PZ in ionic liquid electrolyte is mainly associated with electric double layer capacitive mechanism. Furthermore, the MN-MSCs exhibit much higher current densities than MB-MSCs at the same scan rates. The galvanostatic charging/discharging (GCD) tests further confirmed the performance improvement of MN-MSCs compared with MB-MSCs (Fig. 4b and 4c). The areal and volumetric capacitance of MN-MSCs and MB-MSCs are presented and compared in Fig. 4d and 4e. Under the same current density, the areal capacitance increases with increasing thickness of the electrode, due to the increased amount of electrochemically active material per unit area of the electrode. However, the rate performance of the devices decrease with the increase of their thickness, which may be due to the increase in ion diffusion and transport resistance caused by longer diffusion path and the lower porosity of the thicker electrodes. Fig. 4e shows that the volumetric capacitance of MN-MSCs decreases when the thickness is increased at the same current density. Additionally, when comparing the rate capability of devices with different thicknesses, it is found that the rate performance of the device has almost no relationship with the thickness, which is caused by the same reason mentioned above [32–34].

Notably, MN-MSCs has an excellent areal capacitance of 28.3 mF·cm^{-2} and a volumetric capacitance of 15.7F·cm^{-3} at the current density of 0.2 mA·cm^{-2} and a thickness of 18 μm, both of which are significantly higher than those of MB-MSCs (20.7 mF·cm^{-2} and 11.9F·cm^{-3} at 0.2 mA·cm^{-2}). Remarkably, the areal capacitance of MN-MSCs is much higher than the reported G-MSCs (0.5 mF·cm^{-2} and 2.5F·cm^{-3} at 5 mV·s^{-1}) and phosphorene films (2.7 mF·cm^{-2} and 17.8F·cm^{-3} at 5 mV·s^{-1}) [35]. To date, only a Ni-catecholate-based MOF (Ni-CAT MOF) grown on 3D LSG for MOF-MSCs was reported, which shows an operating voltage of 1.4 V, energy density of 4.1 μWh·cm^{-2}, power density of 7 mW·cm^{-2}, and decent cycling stability (5000 cycles maintaining around 81% ~87%) [36]. The electrochemical performances of some previously reported nanocarbon-based MSCs are presented in Tables S2 and S3 for easy-comparison with the MN-MSCs. It is worth noting that high capacitance of ~8.9 mF·cm^{-2} for MN-MSCs can still be retained at a large scan rate of 1000 mV·s^{-1}. In contrast, MB-MSCs show much lower capacitance of 1.3 mF·cm^{-2} at 1000 mV·s^{-1} (Fig. 5a). At a higher current density of 10 mA·cm^{-2}, MN-MSCs can retain a capacitance of 6.4 mF·cm^{-2}, while MB-MSCs can only maintain a capacitance of 1.4 mF·cm^{-2} (Fig. 5b). To exclude the possibility of excellent performance due to the addition of CNT, we tested the areal capacitances of MSCs with 30% CNT at varied current densities (Fig. 5c),

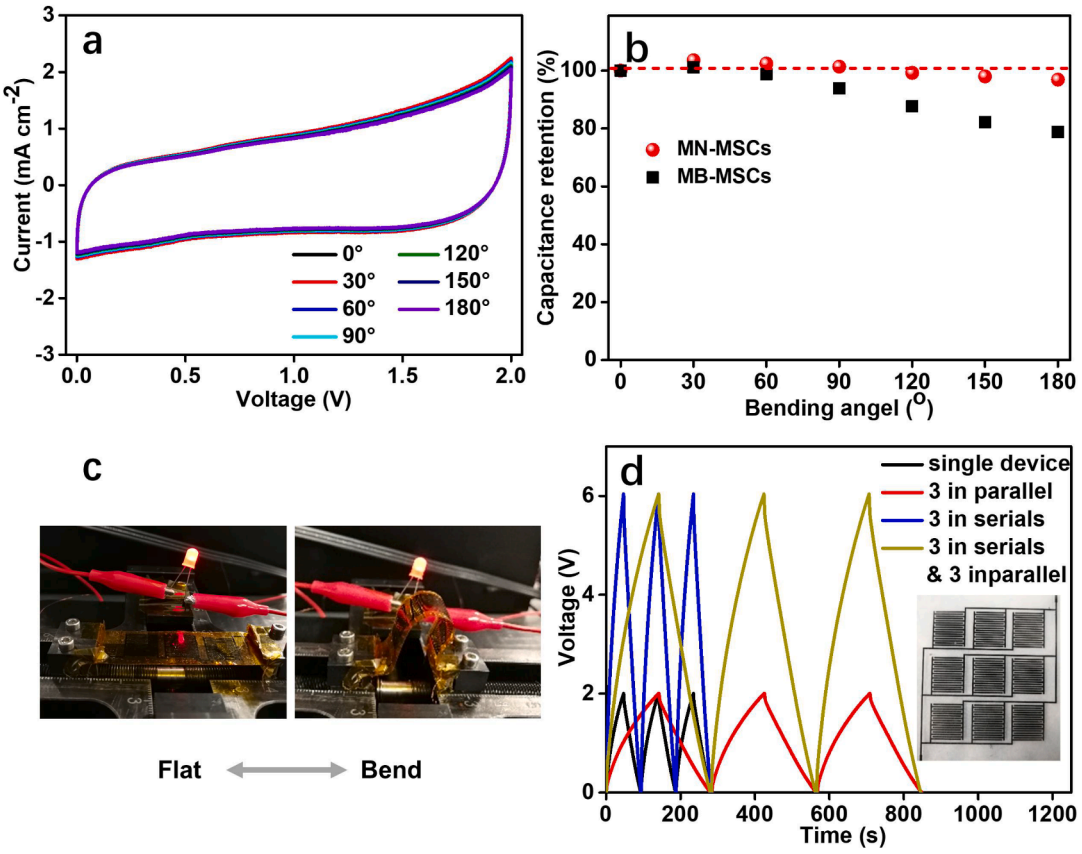

Fig. 6. The flexibility and integration of MN-MSCs. a) CV curves obtained under different bending angles, obtained at 50 mV·s^{-1}. b) Capacitance retention as a function of bending angle of MN-MSCs and MB-MSCs. c) Photographs of a red LED lit up with different bending angles. d) GCD profiles of the MN-MSCs connected in a combination of three series and three parallels tested at 1 mA·cm^{-2}.

proving that increasing the CNT content will not affect the performance. Meanwhile, electrochemical impedance spectra (EIS) show that MN-MSCs have better capacitance behavior than MB-MSCs (Fig. S5). At low frequencies, the slope of MN-MSCs is greater, which is related to the rapid ion transport and capacitive behavior [37]. Based on the fitting results, the equivalent electrolyte resistance (*Rs*) of MN-MSCs is 10.3 Ω, which is much smaller than that of MB-MSCs (16.2 Ω). The *Rs* of MN-MSCs is also lower than that of other materials in the ion electrolyte (270 Ω for phosphorene and graphene-MSCs) [36,38], which further illustrates the excellent electrochemical performance of MN-MSCs. Compared with MB-MSCs (2.4 Ω) electrode, the charge transfer resistance (R_{ct}) of MN-MSCs (0.5 Ω) is significantly lower, indicating that the electrolyte ions diffuse faster in the nanosheet electrodes. This ultrathin construction effectively reduces the contact resistance of the material, which may be because 2D ultrathin CoTCPP-PZ nanosheets are easier to stack into a lamellar structure, thereby reducing electron resistance. Meanwhile, the thinner 2D MOF drastically shortens the ion diffusion paths, contributing to the much lower charge transfer resistance compared with bulk MOF. As the voltage increased to 2.5 V, the electrochemical performance of MN-MSCs showed a certain decline, and the further increase of the voltage caused the oxidation of the solvents (Figs. S6-8). In the evaluation of energy storage device practicability, energy density and power density are critical parameters. The MN-MSCs deliver a high energy density of 8.7 mWh·cm^{-3} at a power density of 110.3 mW·cm^{-3}, and this result exceeds those of most reported carbon-based MSCs, such as 1.8 mWh·cm^{-3} at a power density of 60 mW·cm^{-3} for multi-wall CNT (MWCNT) /Mn_3O_4 MSC [39], and 0.84 mWh·cm^{-3} at a power density of 39.6 mW·cm^{-3} for laser scribed graphene/single-wall CNTs (LSG/SWCNTs) MSC [40]. It is about 40 times higher than carbon/MnO_2 supercapacitor [41], two orders of magnitude higher than ZnO/carbon/MnO_2 supercapacitor [42], which is comparable to commercially available high-energy lithium thin-film battery (4 V/500 μAh) [43], and at least three orders of magnitude higher than high-power aluminum electrolytic capacitor (3 V/300 mF) [44] (Fig. 4f). Meanwhile, after 10,000 cycles at 5 mA·cm^{-2}, MN-MSCs maintain 96.0% of their initial capacitance, which is significantly better than the 77.5% of MB-MSCs (Fig. 5d). Also, the MN-MSCs showed a higher coulombic efficiency (93.2%) than that of MB-MSCs (86.7%), as shown in Fig. 5d. We suggest the morphology is the domain reason. Compared with the loose-stacked 3D MOF bulks, the close-stacked 2D MOF nanosheets contribute to the improved adhesion to the current collector, as well as easy ion migration within the MOF pores for better wettability in less cycles. The internal resistance of MN-MSCs (72.1 Ω) is lower than that of MB-MSCs (119.5 Ω) after cycling test, which further demonstrates the enhanced electrochemical performance of MN-MSCs (Fig. S5). After cycling test, the PXRD patterns have been characterized (Fig. S9), in which the characteristic peaks of CoTCPP-PZ nanosheets at low diffract angle are fully remained, manifesting its excellent structural stability. Moreover, TEM and HRTEM images (Fig. S10) show the flat structure and clear lattice fringe of CoTCPP-PZ nanosheets after cycling test, further demonstrating the stable structure of CoTCPP-PZ nanosheets.

To demonstrate the robust mechanical flexibility of the MN-MSCs, its electrochemical performance under different bending states of 0, 30, 60, 90, 120, 150, 180° is compared. Remarkably, all the CV curves of MN-MSCs overlap almost completely (Fig. 6a). It still maintains 96.9% of the initial capacitance at 0° even when the bending angle reaches 180° (Fig. 6b), while MB-MSCs only maintain 78.8% of the initial capacitance. Thus, MN-MSCs have excellent flexibility and electrochemical stability compared with MB-MSCs. As a demonstration, the flexible MN-MSCs power up a light-emitting diode (LED, Fig. 6c). The easy

integration of MN-MSCs in series and/or parallel can provide desirable output voltage and/or capacitance. As confirmed by the GCD test at 1 $mA{\cdot}cm^{-2}$ (Fig. 6d), the response of MN-MSCs connected in series from 1 to 3 cells was realized. These curves show that the voltage gradually increase linearly from 2.0 to 6.0 V, indicating excellent performance uniformity. Meanwhile, the parallel connection of three MN-MSCs increases the output current by 3 times that of a single cell, while the voltage window remains unchanged. Combining six MN-MSCs with three in series and three in parallel can provide the output voltage of 6.0 V and 3 times the discharge time.

The excellent performance of MN-MSCs can be attributed to the unique properties of 2D ultrathin MOF nanosheets. First, porphyrin ligands with planar semiconductor properties are favorable for the preparation of 2D materials and the fabrication of planar devices. Second, the BET surface area of CoTCPP-PZ nanosheets is significantly higher than that of CoTCPP-PZ Bulk, thus significantly increasing the active surface of the electrode material for MSCs. Third, the production of ultrathin CoTCPP-PZ nanosheets enlarges the electrochemically active surface areas, and makes it easier for the materials to adhere to the flexible planar substrates, thus contributing to the enhanced capacitance, excellent flexibility and stability of MN-MSCs *vs* MB-MSCs. Forth, the interdigital geometry of MSC fully utilizes the advantages of 2D ultrathin nanosheets, enabling the ultrafast entry into the adjacent fingers of electrolyte ions, further shortening the ion diffusion pathways and enabling the efficient charge storage, thereby maximizing the performance of MN-MSCs.

4. Conclusions

In conclusion, we have precisely constructed a new ultrathin MOF nanosheet by controlling the growth of a 3D MOF. Significantly, such MOF nanosheets can be used directly as binder-free flexible electrode films for all-solid-state MSCs through a one-step mask-assisted simplified fabrication method. Compared with MB-MSCs, the resultant MN-MSCs have not only better electrochemical performance, but also impressive uniformity, mechanical flexibility, and excellent modular integration. Therefore, 2D ultrathin MOF nanosheet sets up a bridge between MOF structures and electronics applications, and this strategy of fabricating ultrathin MOF nanosheets described here provides a new avenue to functionalize MOFs for their wide applications in microscale electronics devices.

Declaration of Competing Interest

The authors declare that they have no known competing financial interests or personal relationships that could have appeared to influence the work reported in this paper.

Acknowledgements

This work was supported by the National Natural Science Foundation of China (Grants. 21771191, 21875285, 51872283, 21805273, 22075279), Key Research and Development Projects of Shandong Province (2019JZZY010331), Taishan Scholars Program (ts201511019), the Fundamental Research Funds for the Central Universities (19CX05001A), National Key R&D Program of China (Grants 2016YBF0100100, 2016YFA0200200), LiaoNing Revitalization Talents Program (Grant XLYC1807153), Natural Science Foundation of Liaoning Province, Joint Research Fund Liaoning-Shenyang National Laboratory for Materials Science (Grant 20180510038), DICP (DICP ZZBS201708, DICP ZZBS201802, DICP I202032), DICP&QIBEBT (Grant DICP&QIBEBT UN201702), DNL Cooperation Fund, CAS (DNL180310, DNL180308, DNL201912, DNL201915).

Appendix A. Supplementary data

Supplementary data to this article can be found online at https://doi.org/10.1016/j.cej.2020.127520.

References

[1] W. Gao, N. Singh, L.i. Song, Z. Liu, A.L.M. Reddy, L. Ci, R. Vajtai, Q. Zhang, B. Wei, P.M. Ajayan, Direct laser writing of micro-supercapacitors on hydrated graphite oxide films, Nat. Nanotech. 6 (8) (2011) 496–500.
[2] F.X. Wang, X.W. Wu, X.H. Yuan, Z.C. Liu, Y. Zhang, L.J. Fu, Y.S. Zhu, Q.M. Zhou, Y. P. Wu, W. Huang, Latest advances in supercapacitors: from new electrode materials to novel device designs, Chem. Soc. Rev. 46 (2017) 6816–6854.
[3] H. Hosseini, S. Shahrokhian, Self-supported nanoporous Zn-Ni-Co/Cu selenides microball arrays for hybrid energy storage and electrocatalytic water/urea splitting, Chem. Eng. J. 375 (2019), 122090.
[4] D. Sheberla, J.C. Bachman, J.S. Elias, C.-J. Sun, Y. Shao-Horn, M. Dincă, Conductive MOF electrodes for stable supercapacitors with high areal capacitance, Nat. Mater. 16 (2) (2017) 220–224.
[5] H. Hosseini, S. Shahrokhian, Advanced binder-free electrode based on core-shell nanostructures of mesoporous $Co_3V_2O_8$-$Ni_3V_2O_8$ thin layers@porous carbon nanofifibers for high-performance and flflexible all-solid-state supercapacitors, Chem. Eng. J. 341 (2018) 10–26.
[6] A.C. Forse, J.M. Griffin, C. Merlet, P.M. Bayley, H. Wang, P. Simon, C.P. Grey, NMR study of ion dynamics and charge storage in ionic liquid supercapacitors, J. Am. Chem. Soc. 137 (22) (2015) 7231–7242.
[7] Z. Lv, W. Li, L.e. Yang, X.J. Loh, X. Chen, Custom-made electrochemical energy storage devices, ACS Energy Lett. 4 (2) (2019) 606–614.
[8] F. Hekmat, S. Shahrokhian, N. Taghavinia, Ultralight flexible asymmetric supercapacitors based on manganese dioxide–polyaniline nanocomposite and reduced graphene oxide electrodes directly deposited on foldable cellulose papers, J. Phys. Chem. C 122 (48) (2018) 27156–27168.
[9] Q. Jiang, Y. Lei, H. Liang, K. Xi, C. Xia, H.N. Alshareef, Review of MXene electrochemical microsupercapacitors, Energy Storage Mater. 27 (2020) 78–95.
[10] Z. Lv, Y. Luo, Y. Tang, J. Wei, Z. Zhu, X. Zhou, W. Li, Y.i. Zeng, W. Zhang, Y. Zhang, D. Qi, S. Pan, X.J. Loh, X. Chen, Editable supercapacitors with customizable stretchability based on mechanically strengthened ultralong MnO_2 nanowire composite, Adv. Mater. 30 (2) (2018) 1704531–1704539.
[11] M. Zhao, Y. Huang, Y. Peng, Z. Huang, Q. Ma, H. Zhang, Two-dimensional metal–organic framework nanosheets: synthesis and applications, Chem. Soc. Rev. 47 (16) (2018) 6267–6295.
[12] S. Zhao, Y. Wang, J. Dong, C.-T. He, H. Yin, P. An, K. Zhao, X. Zhang, C. Gao, L. Zhang, J. Lv, J. Wang, J. Zhang, A.M. Khattak, N.A. Khan, Z. Wei, J. Zhang, S. Liu, H. Zhao, Z. Tang, Ultrathin metal-organic framework nanosheets for electrocatalytic oxygen evolution, Nat. Energy 1 (2016) 16184.
[13] Y. Peng, Y. Li, Y. Ban, H. Jin, W. Jiao, X. Liu, W. Yang, Metal-organic framework nanosheets as building blocks for molecular sieve membranes, Science 346 (2014) 1356–1359.
[14] L. Cao, Z. Lin, F. Peng, W. Wang, R. Huang, C. Wang, J. Yan, J. Liang, Z. Zhang, T. Zhang, L. Long, J. Sun, W. Lin, Self-supporting metal-organic layers as single-site solid catalysts, Angew. Chem. Int. Ed. 55 (16) (2016) 4962–4966.
[15] D. Feng, T. Lei, M.R. Lukatskaya, J. Park, Z. Huang, M. Lee, L. Shaw, S. Chen, A. A. Yakovenko, A. Kulkarni, J. Xiao, K. Fredrickson, J.B. Tok, X. Zou, Y.i. Cui, Z. Bao, Robust and conductive two-dimensional metal−organic frameworks with exceptionally high volumetric and areal capacitance, Nat. Energy 3 (1) (2018) 30–36.
[16] J. Liu, Y.i. Zhou, Z. Xie, Y. Li, Y. Liu, J. Sun, Y. Ma, O. Terasaki, L. Chen, Conjugated copper–catecholate framework electrodes for efficient energy storage, Angew. Chem. Int. Ed. 59 (3) (2020) 1081–1086.
[17] L.u. Wang, X. Feng, L. Ren, Q. Piao, J. Zhong, Y. Wang, H. Li, Y. Chen, B.o. Wang, Flexible solid-state supercapacitor based on a metal–organic framework interwoven by electrochemically-deposited PANI, J. Am. Chem. Soc. 137 (15) (2015) 4920–4923.
[18] S. Bi, H. Banda, M. Chen, L. Niu, M. Chen, T. Wu, J. Wang, R. Wang, J. Feng, T. Chen, M. Dincă, A.A. Kornyshev, G. Feng, Molecular understanding of charge storage and charging dynamics in supercapacitors with MOF electrodes and ionic liquid electrolytes, Nat. Mater. 19 (5) (2020) 552–558.
[19] H. Li, Y. Hou, F. Wang, M.R. Lohe, X. Zhuang, L.i. Niu, X. Feng, Flexible all-solid-state supercapacitors with high volumetric capacitances boosted by solution processable MXene and electrochemically exfoliated graphene, Adv. Energy Mater. 7 (4) (2017) 1601847.
[20] Y. Wang, M. Zhao, J. Ping, B.o. Chen, X. Cao, Y. Huang, C. Tan, Q. Ma, S. Wu, Y. Yu, Q. Lu, J. Chen, W. Zhao, Y. Ying, H. Zhang, Bioinspired design of ultrathin 2D bimetallic metal-organic-framework nanosheets used as biomimetic enzymes, Adv. Mater. 28 (21) (2016) 4149–4155.
[21] Y.-Z. Li, Z.-H. Fu, G. Xu, Metal-organic framework nanosheets: preparation and applications, Coord. Chem. Rev. 388 (2019) 79–106.
[22] M. Zhao, Y. Wang, Q. Ma, Y. Huang, X. Zhang, J. Ping, Z. Zhang, Q. Lu, Y. Yu, H. Xu, Y. Zhao, H. Zhang, Ultrathin 2D metal-organic framework nanosheets, Adv. Mater. 27 (45) (2015) 7372–7378.
[23] Y. Huang, M. Zhao, S. Han, Z. Lai, J. Yang, C. Tan, Q. Ma, Q. Lu, J. Chen, X. Zhang, Z. Zhang, B. Li, B. Chen, Y. Zong, H. Zhang, Growth of Au nanoparticles on 2D metalloporphyrinic metal-organic framework nanosheets used as biomimetic catalysts for cascade reactions, Adv. Mater. 29 (2017) 1700102.

[24] A. Pustovarenko, M.G. Goesten, S. Sachdeva, M. Shan, Z. Amghouz, Y. Belmabkhout, A. Dikhtiarenko, T. Rodenas, D. Keskin, I.K. Voets, B. M. Weckhuysen, M. Eddaoudi, L.C.P.M. de Smet, E.J.R. Sudhölter, F. Kapteijn, B. Seoane, J. Gascon, Nanosheets of nonlayered aluminum metal-organic frameworks through a surfactant-assisted method, Adv. Mater. 30 (2018) 1707234.
[25] D.i. Tian, N.a. Song, M. Zhong, X. Lu, C.e. Wang, Bimetallic MOF nanosheets decorated on electrospun nanofibers for high-performance asymmetric supercapacitors, ACS Appl. Mater. Interfaces 12 (1) (2020) 1280–1291.
[26] Y. Ling, H. Chen, J. Zhou, K. Tao, S. Zhao, X. Yu, L. Han, Metal-organosulfide coordination polymer nanosheet array as a battery-type electrode for an asymmetric supercapacitor, Inorg. Chem. 59 (10) (2020) 7360–7369.
[27] X. Zhang, P. Zhang, C. Chen, J. Zhang, G. Yang, L. Zheng, J. Zhang, B. Han, Fabrication of 2D metal–organic framework nanosheets with tailorable thickness using bio-based surfactants and their application in catalysis, Green Chem. 21 (1) (2019) 54–58.
[28] W. Zhao, J. Peng, W. Wang, S. Liu, Q. Zhao, W. Huang, Ultrathin two-dimensional metal-organic framework nanosheets for functional electronic devices, Coord. Chem. Rev. 377 (2018) 44–63.
[29] W.-H. Li, K. Ding, H.-R. Tian, M.-S. Yao, B. Nath, W.-H. Deng, Y. Wang, G. Xu, Conductive metal-organic framework nanowire array electrodes for high-performance solid-state supercapacitors, Adv. Funct. Mater. 27 (27) (2017) 1702067–1702073.
[30] F. Zhou, H.B. Huang, C.H. Xiao, S.H. Zheng, X.Y. Shi, J.Q. Qin, Q. Fu, X.H. Bao, X. L. Feng, K. Müllen, Z.-S. Wu, Electrochemically scalable production of fluorine-modified graphene for flexible and high-energy ionogel-based microsupercapacitor, J. Am. Chem. Soc. 140 (2018) 8198–8205.
[31] V.A. Blatov, A.P. Shevchenko, D.M. Proserpio, Applied topological analysis of crystal structures with the program package ToposPro, Cryst. Growth Des. 14 (7) (2014) 3576–3586.
[32] F. Hekmat, H. Hosseini, S. Shahrokhian, U. Emrah, Hybrid energy storage device from binder-free zinc-cobalt sulfifide decorated biomass-derived carbon microspheres and pyrolyzed polyaniline nanotube-iron oxide, Energy Storage Mater. 25 (2020) 621–635.
[33] L.a. Li, C. Fu, Z. Lou, S. Chen, W. Han, K. Jiang, D.i. Chen, G. Shen, Flexible planar concentric circular micro-supercapacitor arrays for wearable gas sensing application, Nano Energy 41 (2017) 261–268.
[34] S.-K. Kim, H.-J. Koo, A. Lee, P.V. Braun, Selective wetting-induced micro-electrode patterning for flexible micro-supercapacitors, Adv. Mater. 26 (30) (2014) 5108–5112.
[35] H. Xiao, Z.-S. Wu, L. Chen, F. Zhou, S. Zheng, W. Ren, H.-M. Cheng, X. Bao, One-step device fabrication of phosphorene and graphene interdigital micro-supercapacitors with high energy density, ACS Nano 11 (7) (2017) 7284–7292.
[36] H. Wu, W.L. Zhang, S. Kandambeth, O. Shekhah, M. Eddaoudi, H.N. Alshareef, Conductive metal-organic frameworks selectively grown on laser-scribed graphene for electrochemical microsupercapacitors, Adv. Energy Mater. 9 (2019) 1900482.
[37] Z.S. Lv, Y. Tang, Z. Zhu, J. Wei, W. Li, H. Xia, Y. Jiang, Z. Liu, Y. Luo, X. Ge, Y. Zhang, R. Wang, W. Zhang, X.J. Loh, X. Chen, Honeycomb-lantern-inspired 3D stretchable supercapacitors with enhanced specific areal capacitance, Adv. Mater. 30 (2018) 1805468.
[38] J.F. Jover, R. Lugo, H. Toulhoat, P. Simon, T. de Bruin, Screening methodology for the efficient pairing of ionic liquids and carbonaceous electrodes applied to electric energy storage, J. Phys. Chem. C 118 (2) (2014) 864–872.
[39] G. Lee, D. Kim, D. Kim, S. Oh, J. Yun, J. Kim, S.-S. Lee, J.S. Ha, Fabrication of a stretchable and patchable array of high performance micro-supercapacitors using a non-aqueous solvent based gel electrolyte, Energy Environ. Sci. 8 (6) (2015) 1764–1774.
[40] F. Wen, C. Hao, J. Xiang, L. Wang, H. Hou, Z. Su, W. Hu, Z. Liu, Enhanced laser scribed flexible graphene-based micro-supercapacitor performance with reduction of carbon nanotubes diameter, Carbon 75 (2014) 236–243.
[41] X.u. Xiao, T. Li, P. Yang, Y. Gao, H. Jin, W. Ni, W. Zhan, X. Zhang, Y. Cao, J. Zhong, L.i. Gong, W.-C. Yen, W. Mai, J. Chen, K. Huo, Y.-L. Chueh, Z.L. Wang, J. Zhou, Fiber-Based All-Solid-State Flexible Supercapacitors for Self-Powered Systems, ACS Nano 6 (10) (2012) 9200–9206.
[42] P. Yang, X.u. Xiao, Y. Li, Y. Ding, P. Qiang, X. Tan, W. Mai, Z. Lin, W. Wu, T. Li, H. Jin, P. Liu, J. Zhou, C.P. Wong, Z.L. Wang, Hydrogenated ZnO core–shell nanocables for flexible supercapacitors and self-powered systems, ACS Nano 7 (3) (2013) 2617–2626.
[43] D. Pech, M. Brunet, H. Durou, P. Huang, V. Mochalin, Y. Gogotsi, P.-L. Taberna, P. Simon, Ultrahigh-power micrometre-sized supercapacitors based on onion-like carbon, Nat. Nanotech. 5 (9) (2010) 651–654.
[44] M.F. El-Kady, V. Strong, S. Dubin, R.B. Kaner, Laser scribing of high-performance and flexible graphene-based electrochemical capacitors, Science 335 (6074) (2012) 1326–1330.